Journal of Applied Physics

Electrical and structural properties of binary Ga–Sb phase change memory alloys

Cite as: J. Appl. Phys. **132**, 035103 (2022); https://doi.org/10.1063/5.0096022
Submitted: 14 April 2022 • Accepted: 28 June 2022 • Published Online: 18 July 2022

Rubab Ume, Haibo Gong, Vadim Tokranov, et al.

Journal of Applied Physics Special Topics Open for Submissions
Learn More

© 2022 Author(s).

Journal of Applied Physics | ARTICLE | scitation.org/journal/jap

Electrical and structural properties of binary Ga–Sb phase change memory alloys

Cite as: J. Appl. Phys. **132**, 035103 (2022); doi: 10.1063/5.0096022
Submitted: 14 April 2022 · Accepted: 28 June 2022 ·
Published Online: 18 July 2022

View Online

Export Citation

CrossMark

Rubab Ume,[1,a)] Haibo Gong,[1] Vadim Tokranov,[1] Michael Yakimov,[1] Kevin Brew,[2] Guy Cohen,[3] Christian Lavoie,[3] Sandra Schujman,[1] Jing Liu,[4] Anatoly I. Frenkel,[5,6] Karsten Beckmann,[1] Nathaniel Cady,[1] and Serge Oktyabrsky[1]

AFFILIATIONS

[1]SUNY Polytechnic Institute, 257 Fuller Road, Albany, New York 12203, USA
[2]IBM AI Hardware Center, 257 Fuller Road, Albany, New York 12309, USA
[3]IBM T.J. Watson Research Center, 1101 Kitchawan Road, Yorktown Heights, New York 10598, USA
[4]Department of Physics, Manhattan College, Riverdale, New York 10471, USA
[5]Department of Materials Science and Chemical Engineering, Stony Brook University, Stony Brook, New York 11793, USA
[6]Chemistry Division, Brookhaven National Laboratory, Upton, New York 11973, USA

[a)]**Author to whom correspondence should be addressed:** umer@sunypoly.edu

ABSTRACT

Material properties of Ga–Sb binary alloy thin films deposited under ultra-high vacuum conditions were studied for analog phase change memory (PCM) applications. Crystallization of this alloy was shown to occur in the temperature range of 180–264 °C, with activation energy >2.5 eV depending on the composition. X-ray diffraction (XRD) studies showed phase separation upon crystallization into two phases, Ga-doped A7 antimony and cubic zinc-blende GaSb. Synchrotron *in situ* XRD analysis revealed that crystallization into the A7 phase is accompanied by Ga out-diffusion from the grains. X-ray absorption fine structure studies of the local structure of these alloys demonstrated a bond length decrease with a stable coordination number of 4 upon amorphous-to-crystalline phase transformation. Mushroom cell structures built with Ga–Sb alloys on ø110 nm TiN heater show a phase change material resistance switching behavior with resistance ratio >100 under electrical pulse measurements. TEM and Energy Dispersive Spectroscopy (EDS) studies of the Ga–Sb cells after ∼100 switching cycles revealed that partial SET or intermediate resistance states are attained by the variation of the grain size of the material as well as the Ga content in the A7 phase. A mechanism for a reversible composition control is proposed for analog cell performance. These results indicate that Te-free Ga–Sb binary alloys are potential candidates for analog PCM applications.

Published under an exclusive license by AIP Publishing. https://doi.org/10.1063/5.0096022

I. INTRODUCTION

Phase change memory (PCM) alloys have shown great promise for non-volatile memory and data storage devices due to their fast switching, high endurance, and excellent scaling properties.[1–4] Currently, $Ge_2Sb_2Te_5$ (GST) has been the primary material of PCM technology with applications ranging from optical and electronic storage devices and embedded memory applications as well as neuromorphic applications.[5–8] However, the presence of volatile Te and elemental redistribution during programming in these intermetallic alloys can cause poor thermal stability and data retention.[9–11] It has been shown that tellurium-poor Ge–Sb–Te compounds show enhanced data retention and increase in activation energy of crystallization and, therefore, leading to an interest in Te-free cells.[12] To avoid compositional changes during programming a simplest material, a single element Sb has also been demonstrated as a phase change material through ultrafast cooling from the melt.[13] The recent emphasis of PCM technology development is on improving variability and stability, reducing power consumption, and controllable multilevel storage for analog memory. Te-free binary alloys of Sb-rich materials with group III and IV elements have been studied and have shown faster crystallization and improved stability as compared to GST.[14–19] Moreover, PCM materials typically demonstrate 5%–6% mass density change upon phase transformation, which can cause void formation in the PCM cell leading to device failure.[14,20,21]

Published under an exclusive license by AIP Publishing

Remarkably, $Ga_{0.3}Sb_{0.7}$ alloy was reported to have zero density change, thus potentially improving cell stability.[14] Additionally, Ge-, Al-, and Ga-doped Sb-based alloys have demonstrated high archival lifetime and amorphous phase stability.[14,22,23] Ga–Sb along with Al–Sb, which has also demonstrated high-resistance contrast,[23] can be combined to form alternating stacked nanolayers to form phase change heterostructure (PCH) that in some cases can demonstrate lower noise and drift to allow for reliable switching operations.[24] Therefore, this work focuses on studying the electrical and structural properties of amorphous and crystalline phases of Ga–Sb-based alloys with different Ga compositions for their potential in multilevel and analog memory devices.

II. MATERIALS AND METHODS

For bulk material studies, Ga–Sb amorphous layers were deposited in a molecular beam epitaxy (MBE) reactor under an ultra-high vacuum of $\sim 7 \times 10^{-11}$ Torr at 20 °C on Si substrates with 1 μm thick thermally grown SiO_2. The film compositions were confirmed by *in situ* Auger electron spectroscopy. These films were further capped *in situ* with a 20 nm of Al_2O_3 to prevent oxidation of the alloys. Ga–Sb layers of different thicknesses and compositions were deposited at room temperature in order to prevent possible composition variations. PCM mushroom cells with patterned ø110 nm TiN bottom electrode heaters in a SiN dielectric layer were fabricated on templates prepared in a Si foundry. For mushroom cell devices, a 30–50 nm TaN top electrode layer was deposited on the blanket PCM using *in situ* magnetron sputtering in a separate chamber connected to the MBE reactor. PCM cells were completed with optical lithography and dry/wet etching to pattern the top contact pads and PCM layers to separate individual cells.

The change in resistance as a function of temperature at a constant heating rate was measured with a two-point probe setup on a hot plate in air. Resistivity values were further obtained via a Van der Pauw geometry to measure sheet resistivity of the PCM. The crystallization temperature and activation energy were determined from the sheet resistance vs temperature curves. The same setup was used to evaluate resistance change with time at a fixed temperature for obtaining data retention. *In situ* synchrotron XRD data at Canadian Light Source and *ex situ* XRD methods were used to study the nucleation and crystallization behavior of the Ga–Sb alloys. That study provided data on the crystal phases as well as their relative fraction in the films. X-ray absorption fine structure (XAFS) spectroscopy at the Ga K-edge at the QAS beamline of National Synchrotron Light Source—II at Brookhaven National Laboratory was used to study the atomic arrangement changes upon amorphous-to-crystalline transformation. Transmission electron microscopy (TEM) provided quantitative information on the grain size, crystallization behavior, and redistribution of elements. Electrical performance of the PCM cells was analyzed with electrical pulse and DC measurements, which provided the RESET/SET resistance ratio and programming performance of the cells for analog resistive memory applications.

III. RESULTS

A. Thermo-electrical analysis

Figure 1(a) shows sheet resistivity as a function of temperature for 160 nm thick Ga–Sb films with different compositions. The as-deposited samples were amorphous, consistent with the high resistivity of the films. The initial room temperature resistivity of amorphous films increased with a higher Ga fraction; upon annealing the resistance of all Ga–Sb films decreased with a sharp drop at the crystallization temperature (T_C) corresponding to amorphous to crystalline phase transformation. Additionally, the samples with 20%–40% Ga show an increase in resistance with temperatures beyond T_C, potentially due to a highly doped degenerate GaSb phase. Alloying Ga with Sb increases both the amorphous and crystalline state resistances as shown in Fig. 1(b). Activation energies of amorphous phase conductivity (E_σ) extracted from the R-T data demonstrate an increase of E_σ at higher Ga concentration [Fig. 1(c)], which is likely due to mobility gap modulation with doping.[25] The observed reduction of the resistivity in the Sb-rich amorphous samples is likely related to the presence of more metallic Sb contributing to the properties of relatively resistive amorphous $Ga_{0.5}Sb_{0.5}$ with a specific resistivity of 20–100 Ω cm.[26] In the crystallized state, resistivity is due to metallic Sb and is still low in Ga-rich alloy because crystalline semiconducting GaSb is typically of p-type due to Fermi level pinning on defects and interfaces.[27]

Sheet resistivity measurements as shown in Fig. 1(a) were obtained for different heating rates, and corresponding crystallization temperatures were calculated for different compositions. The dependence of crystallization temperature T_C as a function of Ga content at various heating rates along with similarly processed GST PCM alloy for comparison is shown in Fig. 1(d). The T_C increases with increasing Ga concentration reaching a maximum value of 264 °C for 30% of Ga followed by a fast drop in T_C at higher Ga contents possibly corresponding to the crystallization of GaSb phase as shown later. The composition dependent T_C for Ga–Sb films up to 40% of Ga concentration is higher than that of GST (173–188 °C) and is expected to result in better thermal stability for Ga–Sb-based PCM devices. Higher Tc can also lead to higher SET state current causing higher power consumption. Measured T_C values increased at higher heating rates and this dependence was used to calculate the activation energy of crystallization using the Kissinger method.[28] The activation energies shown in Fig. 1(e) for Ga–Sb ranged from 0.9 to 2.5 eV with reduced values exhibited in alloys with Ga contents above 30 at. %. The extrapolated failure times for these Ga–Sb films show improved data retention over GST as depicted in Fig. 1(f). Sb as a monoatomic phase change material fabricated into nanometric dimensions to dissipate the heat from a small volume of molten Sb has also been shown to demonstrate about 2.5 orders of magnitude resistance change upon rapid cooling of the molten Sb state.[13] Further confinement of the Sb also demonstrated improved robustness against crystallization.[13] Modification by alloying has also been proven to be an effective approach in enhancing PCM performance.[29] Alloying of GeTe and GST as well as Te-free phase change material has demonstrated significantly higher crystallization temperature (186–237 °C) and activation energy as high as 4.5 eV.[29] This work based on simple binary Ga–Sb alloy provides the data on the effect of composition change on the properties of PCM material to demonstrate widely controllable crystallization temperature and activation energies.

Published under an exclusive license by AIP Publishing

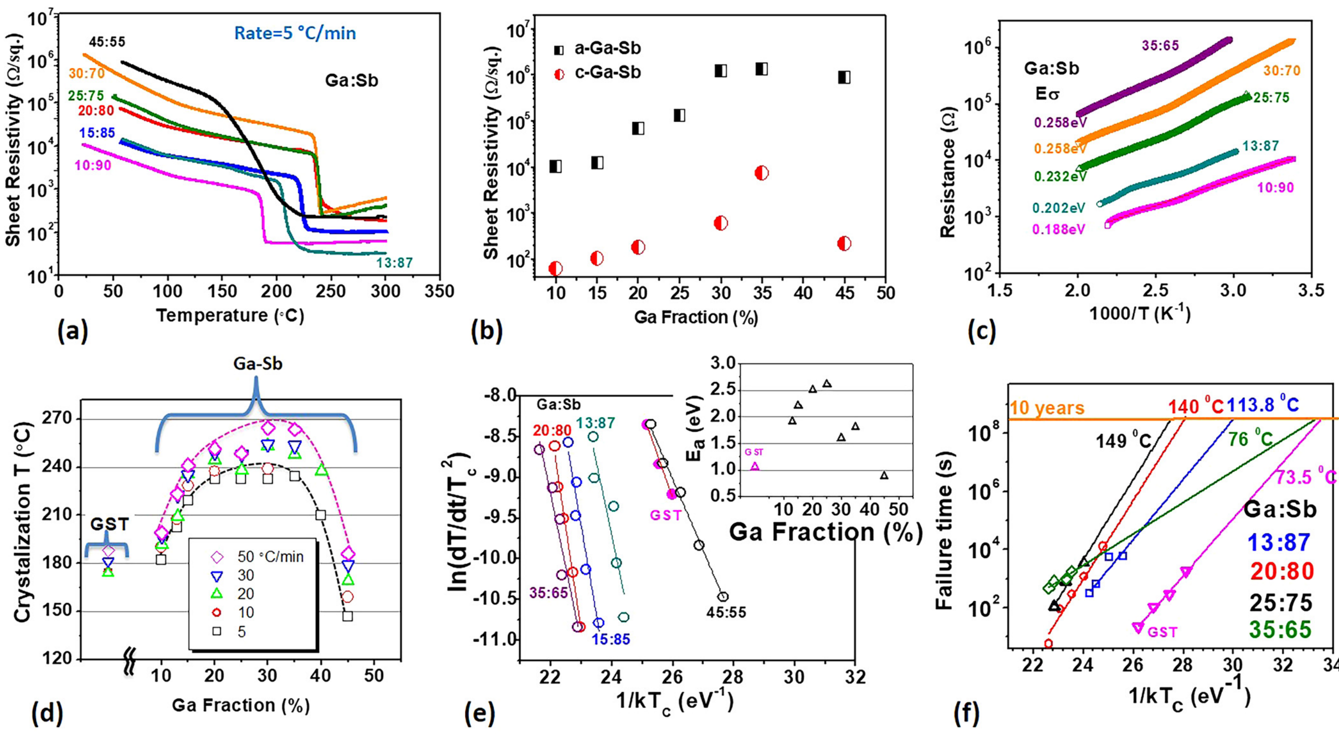

FIG. 1. (a) Sheet resistivity as a function of the temperature of as-grown amorphous Ga–Sb alloy films with various Ga fractions for a heating rate of 5 °C/min. (b) Room temperature sheet resistivity of as-grown amorphous and crystalized 160 nm thick Ga–Sb films with different compositions. (c) Arrhenius plots of conductivity in amorphous state extracted from (a) showing a gradual increase in activation energy (E_σ) with Ga concentration. (d) Crystallization temperature dependence on Ga content at various heating rates. T_C of similarly processed GST PCM alloy is shown for comparison. (e) The Kissinger plots (temperature in K, time in seconds) showing the variation of T_C with heating rate; slopes provide crystallization activation (E_a) plotted in the inset. (f) Arrhenius extrapolation at a ten year data retention.

B. Crystallization of Ga–Sb alloys

Figure 2(a) shows the grazing angle x-ray diffraction (XRD) patterns of Ga–Sb alloy films with different compositions capped with 10 nm thick Al_2O_3 layers, annealed on a hot plate in air at 300 °C with a heating rate of 20 °C/min and then cooled down to room temperature. The as-deposited films were amorphous with no distinct diffraction peaks (not shown here) and the annealed films indicate crystallization into two phases that coexist, a rhombohedral A7 antimony phase[30] and a cubic zinc-blende (ZB) GaSb phase as observed previously.[25,31–33] Simulated diffraction patterns of these two phases are also shown in Fig. 2(a) for reference. The fraction of GaSb cubic phase naturally increases at a higher Ga fraction as indicated by the growth of zinc-blende diffraction peak intensities and diminishing of peaks corresponding to the A7 phase. To quantify the relative volumes of two phases in the films, areas under the (111) GaSb and (012) A7 Sb peaks were calculated from the diffraction data under assumptions that the material is entirely crystallized, GaSb grains are stoichiometric, and the excess Ga is dissolved in the A7 phase and plotted in Fig. 2(b). To improve the accuracy of these calculations the weaker overlapping peaks (101) A7 and (002) ZB, respectively, were also taken into account. These fraction volumes were then compared with the estimated ones obtained under the same assumptions with various Ga dissolved levels. This comparison [Fig. 2(b)] implies that the A7 grains can contain up to about 10% of Ga. An evident deviation of the data points from the model curves at high Ga content is likely related to distortions of the A7 phase due to alloying and reduction of diffraction intensities with respect to the calculated ones that assumed perfect A7 crystal structure. The 10% of Ga in the A7 grains is much higher than the equilibrium solubility of Ga in Sb, which is much less than 1% even at the melting temperature.[32] This high fraction of Ga implies that there is a strong non-equilibrium state of the Ga–Sb alloy in the low-resistance crystalline state.

In situ XRD analysis was carried out during annealing of as-grown amorphous Ga–Sb alloys with the synchrotron light source to further understand their crystallization behavior. Figures 3(a)–3(c) confirm the co-existence of the two phases, A7 Sb and ZB GaSb. The diffraction peaks sharpen with annealing after nucleation as grains grow in size as shown in Fig. 4(a). The evolution of grain sizes of A7 and cubic ZB phases during the *in situ* annealing were obtained using the Scherrer method from $(012)_{A7}$ and $(111)_{ZB}$ peak widths, respectively. The arrows indicate temperatures of crystallization of two phases for the resistance drop for two samples at approximately the same heating rate of

Published under an exclusive license by AIP Publishing

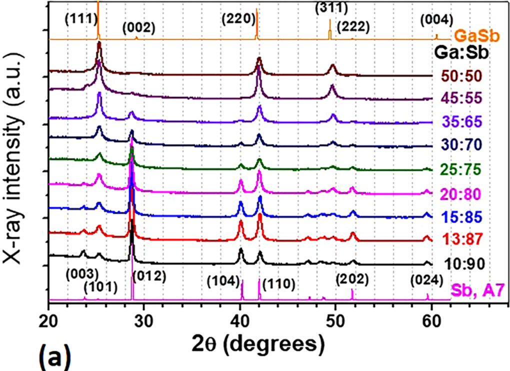

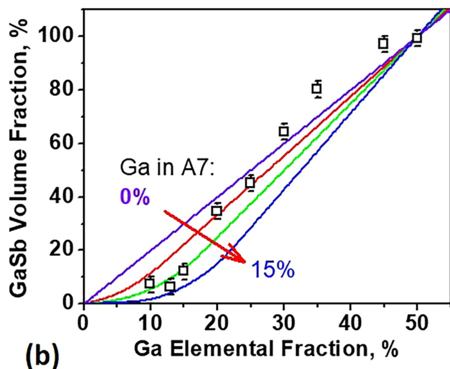

FIG. 2. (a) Grazing angle XRD patterns of Ga–Sb films with variable Ga concentration annealed at 300 °C. Two simulated patterns are shown for the Sb A7 phase (bottom) and the zinc-blende GaSb phase (top). (b) Volume ratios of the zinc-blende GaSb phase calculated from the XRD patterns. Lines present the expected GaSb volumes when the solubility of Ga in the A7 Sb phase is 0, 5, 10, and 15 at. %.

~50 K/min [Fig. 1(d)]. The transition temperature of the $Ga_{0.1}Sb_{0.9}$ alloy coincides with the nucleation of the A7 phase. Therefore, the PCM low-resistance state is related to the crystallization of the A7 phase, where the grains nucleate and remain below about 14 nm in size in the interval of 200–300 °C [Fig. 4(a)].

Sb-rich films with Ga content below 30% demonstrate crystallization of the A7 Sb phase before the GaSb phase while in the $Ga_{0.3}Sb_{0.7}$ alloy, both phases crystalize at the same temperature [Fig. 3(b)]. Further increase of the Ga content results in reversing the sequence of phase crystallization; the $Ga_{0.5}Sb_{0.5}$ sample has noticeable broad peaks at as low as 100 °C, and gradual grain growth [Fig. 4(a)] with grain sizes remaining very small (<10 nm) up to 300 °C when grains of the A7 phase first appear. It should be noted that this gradual growth beginning at lower temperatures is mirrored in the resistance-temperature curves of the $Ga_{0.45}Sb_{0.55}$ sample, which also appears to gradually decrease in contrast to the Sb-rich samples with sharp transitions [Fig. 1(a)]. Figure 4(d) demonstrates that the resistance drop in the Ga–Sb PCMs can be caused by crystallization of either the A7 or ZB phase, whichever occurs first at various amorphous alloy compositions but the ZB phase grows significantly slower and results in slower R(T) transition.

There is also a visible change in the interplanar spacing, particularly in the (110) and (202) planes shown in Fig. 3(a) for $Ga_{0.1}Sb_{0.9}$. These distortions were used to calculate the unit cell volume change upon annealing [Fig. 4(b)]. The solid curves present the unit volumes change due to thermal expansion and were obtained from the same *in situ* XRD runs while cooling down the samples. The measured thermal expansion coefficient for the ZB phase is $7.3 \times 10^{-6}\,K^{-1}$ and is significantly anisotropic for the

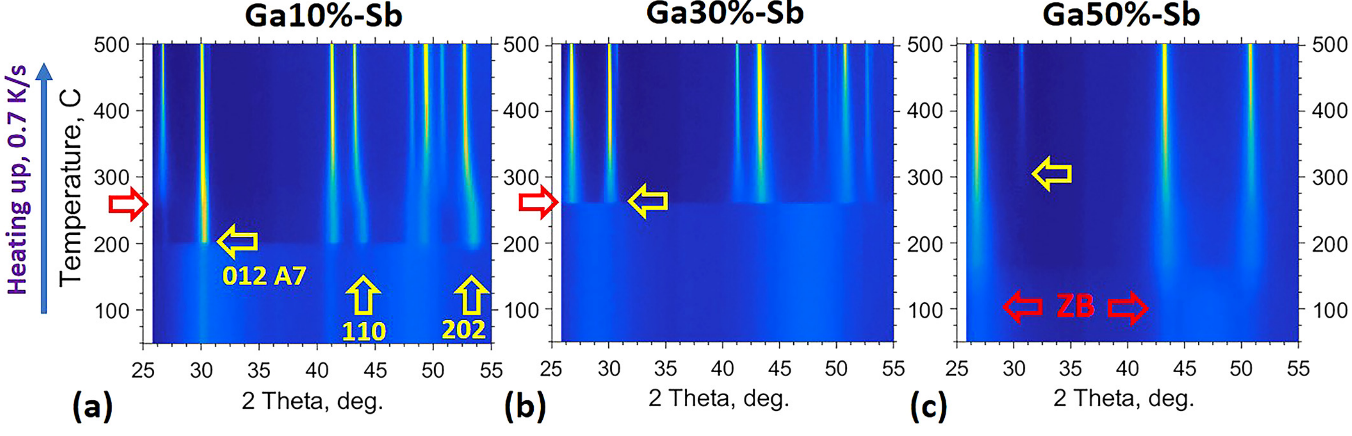

FIG. 3. *In situ* x-ray synchrotron diffraction pattern evolution [(a)–(c)] with annealing of as-grown amorphous alloys at 40 °C/min rate of $Ga_{0.1}Sb_{0.9}$, $Ga_{0.3}Sb_{0.7}$, and $Ga_{0.5}Sb_{0.5}$ compositions. Arrows mark the appearance of XRD reflections of two crystal phases: A7 (Sb-like) and cubic zinc-blende (ZB) GaSb.

Published under an exclusive license by AIP Publishing

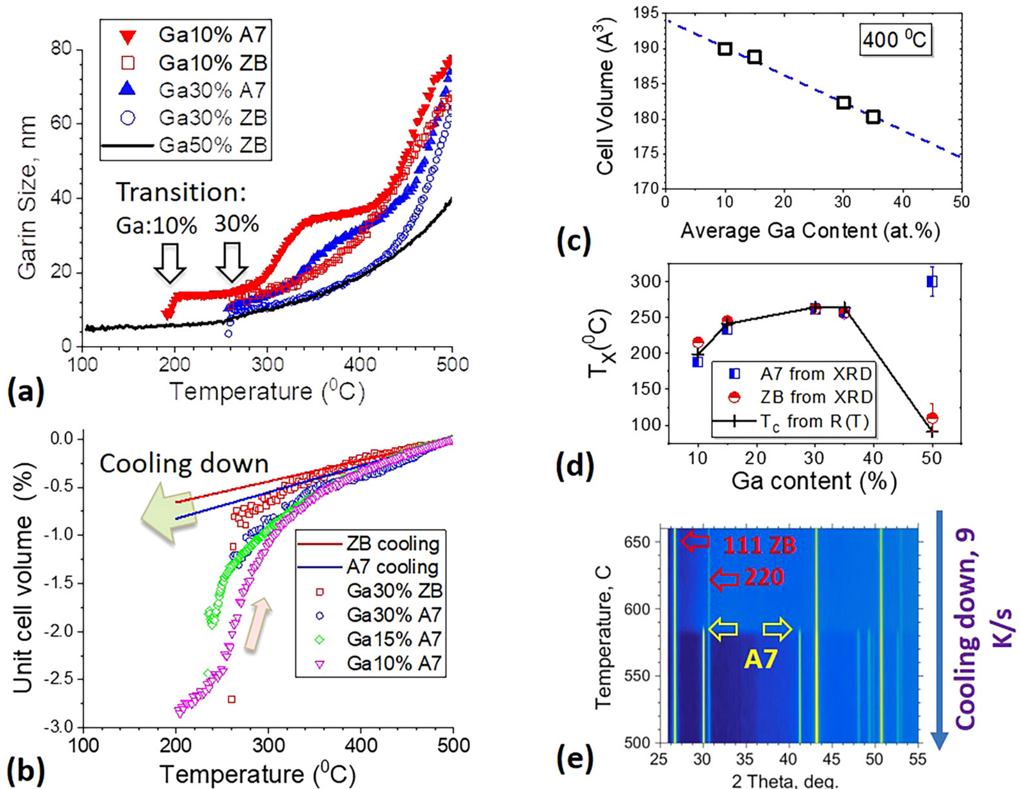

FIG. 4. Synchrotron *in situ* XRD results: (a) crystal size evolution with temperature from XRD reflection broadening using the Scherrer method: (012) for A7 and (111) for cubic GaSb phase. (b) Unit cell volume change upon annealing for different Ga concentrations as well as volume change due to thermal expansion obtained from the cooling-down curves. (c) Unit cell volume of the A7 phase at 400 °C obtained from the crystallization curves for (102) and (104) reflections. (d) Crystallization temperatures of two phases extracted from *in situ* XRD and from resistance vs temperature 50 °C/min heating rate. (e) *In situ* x-ray synchrotron diffraction pattern evolution of $Ga_{0.3}Sb_{0.7}$ upon cooling down from 700 °C showing crystalline ZB phase and crystallization of A7 phase at 585 °C.

A7 phase: $(6.3 \pm 1.0) \times 10^{-6}$ and $(15.8 \pm 1.8) \times 10^{-6}\,K^{-1}$ for hexagonal *a* and *c* axes, respectively.

The unit cell volume change of the A7 phase shows two distinct intervals, most noticeably in the samples with 10 and 15 at. % Ga. The initial interval between 200 and 300 °C reveals a very strong unit volume expansion of over 2%. This change coincides with the region of stable grain size in Fig. 4(a) ruling out size- and strain-related effects. The curves in Figs. 4(a) and 4(b) show different starting temperatures corresponding to the nucleation points for different compositions. Moreover, the unit cell volume of the A7 phase depends also on the alloy composition. Figure 4(c) shows the cell volume reduction at higher Ga concentration when all the phases are crystallized into large 20–40 nm grains. Thus, the most likely reason for the unit volume expansion of the A7 Sb phase with temperature [Fig. 4(a)] is the change in the chemical composition of the A7 grains, namely, an increase in Ga concentration, which will be further discussed in Secs. III C–III E.

Figure 4(e) shows x-ray diffraction of the alloy upon relatively fast cooling down ~9 K/s from about 700 °C. The melting point of GaSb is 712 °C, and the ZB grains stay crystallized in the temperature interval shown. As the pure Sb melting point is 631 °C, the observed crystallization of the A7 phase at about 585 °C in both Ga 10% (not shown) and 30% samples is likely due to Ga-oversaturation in the A7 phase. The wide interval (over 100 °C) between melting/crystallization temperatures of the two phases may provide the medium where the PCM transitions occur by change the state of just the Sb-rich low-melting point phase keeping the ZB phase crystalline at all times. Confining the Sb domains with zinc-blende GaSb would limit carrier mobility and increase resistance.

C. Amorphous structure and bonding transformation

XAFS spectroscopy at National Synchrotron Light Source at Brookhaven National Laboratory was employed to investigate the local structure and bonding changes upon phase transformation from amorphous to crystalline Ga–Sb alloys with different compositions. Figure 5(a) shows the sheet resistivity vs temperature curves for 160 nm thick as-deposited amorphous films. The symbols on the curves represent the resistivity and annealed temperature points of five samples of each composition studied by XAFS at room temperature. The samples were annealed to different temperatures and

Published under an exclusive license by AIP Publishing

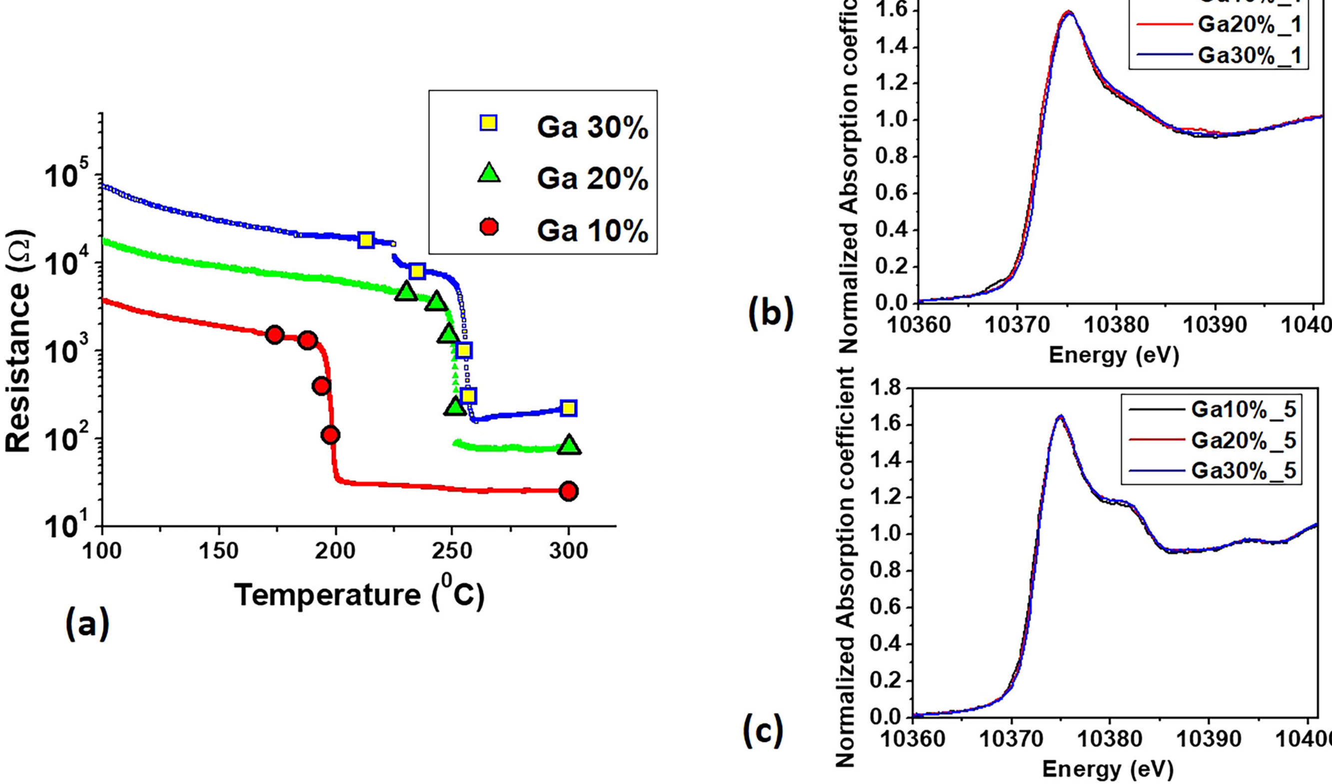

FIG. 5. (a) Ga–Sb crystallization curves for three Ga–Sb films with variable Ga concentration. The symbols show the resistivity of Ga–Sb samples used for XAS studies. (b) and (c) XANES regions of the three films annealed (b) below transition corresponding to the left-most points on each curve in (a) and (c) annealed at 300 °C.

then cooled down to room temperature. Figures 5(b) and 5(c) compare x-ray absorption near edge structure (XANES) of the three alloys annealed at below and above the crystallization temperatures. The spectra demonstrate a clear difference between the amorphous and crystal phases, the latter featuring oscillations of the absorption coefficient in the extended energy range due to medium range order

The extended XAFS (EXAFS) at the Ga K-edge was quantitatively analyzed using ARTEMIS software,[34,35] and the results are summarized in Fig. 6. The fitting model included only Ga–Sb bonds, sufficient for a good fit; Ga–Ga pairs could only be found in the $Ga_{0.3}Sb_{0.7}$ amorphous sample, but with a coordination number as low as 0.3. Homopolar Ga–Ga bonds were previously found in amorphous $Ga_{0.5}Sb_{0.5}$ alloys[36] that further assume the chemical ordering of bonds.

Ga–Sb bond length [Fig. 6(a)] decreases upon amorphous-to-crystalline phase transformation quite similarly for all the samples. The radial distance is reduced by as much as 1.9% in the $Ga_{0.1}Sb_{0.9}$ alloy and about 1% in two other films reaching 2.64 Å in the annealed samples, which correspond to the length of sp^3 bonds in ZB GaSb. Furthermore, the coordination number is close to 4 in all the samples and does not change with annealing keeping the local atomic arrangement of Ga atoms tetrahedral [Fig. 6(b)]. The fourfold coordination number of Ga in Ga–Sb alloys was previously reported,[33,36–38] though threefold coordination of Ga in as-deposited amorphous $Ga_{0.16}Sb_{0.84}$ alloy was also observed.[39] In this work, however, both 10% and 30% Ga samples exhibit clear fourfold tetrahedral bonding of Ga.

The A7 phase is a slightly deformed rhombohedral primitive cubic structure where hexagonal atomic layers are grouped in pairs [Fig. 6(c)]. This results in threefold bonding of Sb atoms with a bond length of about 2.9 Å and significantly longer bonds of 3.3 Å to other three atoms of the parent primitive cubic lattice. This arrangement is somewhat like the ZB structure where hexagonal double layers consist of alternating Ga and Sb planes. The individual hexagonal planes are almost the same in both structures with an atomic spacing of about 4.3 Å between the atoms within the plane. Therefore, Ga impurity with tetrahedral bonding will substitute the Sb atom in the A7 phase keeping three bonds almost intact and rearranging other three weakly bonded Sb atoms to form the sp^3 motif.

Due to different packing of the bilayers as demonstrated in Fig. 6(c), the atomic density of the ZB GaSb phase is 4.5% higher than the A7 Sb phase with a volume per atom of 28.6 vs

Published under an exclusive license by AIP Publishing

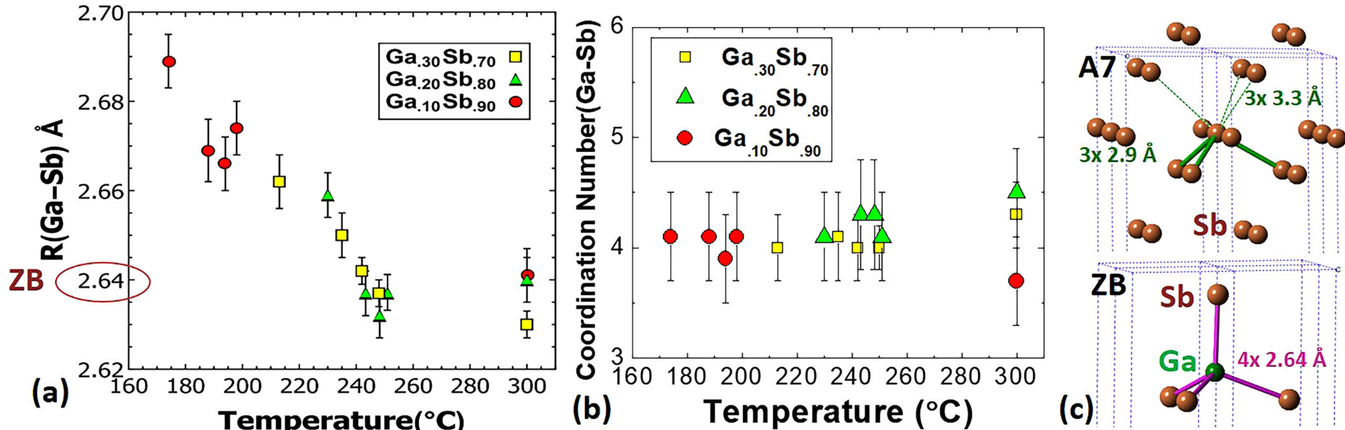

FIG. 6. (a) Ga–Sb distance R(Ga–Sb) as a function of annealing temperature for samples shown in Fig. 4(a). The graph shows Ga–Sb distances close to tetrahedral sp^3 at 2.64 Å. (b) Coordination number of Ga–Sb as a function of annealing temperature for various Ga fractions. (c) Atomic arrangement in rhombohedral Sb A7 phase and tetrahedral bonding in cubic GaSb ZB phase. Both structures are aligned with a vertical hexagonal *c* axis. Bonds of single atoms are shown; for the A7 phase, the threefold coordination consists of three shorter bonds while three longer bonds marked are dashed.

30.0 Å^3/atom, respectively. Hence, Ga tetrahedrally bonded with Sb defects will likely reduce the average unit cell volume of the A7 phase when it crystallizes with high oversaturation with Ga impurities. As shown above in Figs. 4(a) and 4(b), crystallization of the A7 phase has an interval with strong expansion of the unit cell volume without the growth of the crystalline grains, which now can be explained by homogenization of the A7 grains with the expulsion of excess Ga toward the boundaries with amorphous phase.

It is also important to mention another quite obvious conclusion from this discussion. As shown in Ref. 14, the change in an average density of material upon crystallization alters from an increase in Sb-rich alloys to zero in $Ga_{0.3}Sb_{0.7}$ and further to a decrease of the density in the crystalline phase. Thus, the atomic density of the amorphous phase is increasing with Ga alloying stronger than its A7 crystalline counterpart in Fig. 4(c). This corresponds to significantly less than average Ga content in the A7 phase due to the formation of the cubic GaSb grains with even high atomic density. As a result, at 30% average Ga content, the amorphous phase density equalizes the average density of the A7 and ZB phases weighted by their relative volumes. In other words, the zero density change upon crystallization is due to Ga migration from crystallizing A7 phase to the ZB GaSb grains.

D. Electrical analysis Ga–Sb PCM cells

To evaluate reversible switching of Ga–Sb alloys, Ga–Sb films of different compositions were deposited onto Si foundry-prepared templates containing ø110 nm TiN heaters. A mushroom-type device with Ga–Sb PCM layer and *in situ* deposited TaN top metal contact is shown in Fig. 7(a). Figures 7(b) and 7(c) demonstrate reversible switching of $Ga_{0.2}Sb_{0.8}$ and $Ga_{0.4}Sb_{0.6}$ cells between the low-resistance SET and high-resistance RESET states. Higher Ga

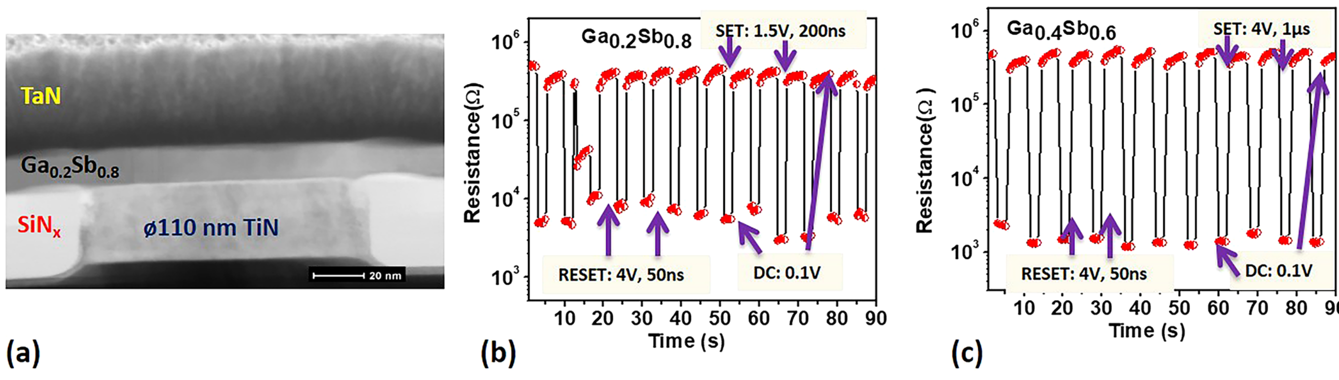

FIG. 7. (a) Bright filed TEM of PCM cell device with ∼16 nm $Ga_{0.2}Sb_{0.8}$ PCM film. (b) and (c) Reversible switching characteristic of $Ga_{0.2}Sb_{0.8}$ and $Ga_{0.4}Sb_{0.6}$, respectively, rising and trailing slopes were 10 ns for SET and 5 ns for RESET pulses.

Published under an exclusive license by AIP Publishing

content leads to larger resistance contrast and also requires more energy as shown by the longer pulse duration for $Ga_{0.4}Sb_{0.6}$ cell to obtain a maximum dynamic range of resistance. It also shows the resistance contrast of about 500 as compared to ∼100 for Ga–Sb alloys with lower Ga content as well as similar to the previously reported performance of Ga–Sb, GST, and other Te-free PCM.[39,43–46]

R–V programming curves of a 16 nm thick $Ga_{0.4}Sb_{0.6}$ mushroom device deposited in the amorphous state for fixed pulse widths are shown in Fig. 8(a). Each point in the graphs was obtained with prior initialization with RESET pulse at 5 V, 50 ns width. The low-resistance SET programming state appears with the increase of pulse amplitude over about 1 V for different pulse widths. The device does not reach a complete crystalline low-resistance state for shorter pulses. Longer pulses of 1 μs are needed for complete SET with a pulse voltage of ∼3.5–4 V. The 1 μs pulse width to obtain a full dynamic resistance range is longer than the ∼50–200 ns widths to switch GST and other Te-free PCM, which could be due to lower thickness resulting in faster thermal relaxation.[43–46] The switching voltages for the SET state are within the range of 1–3 V of previously studied PCM.[43–46] An endurance test is illustrated in Fig. 8(b) for 10^6 cycles with relatively high pulse energy and shows small degradation of the amorphous phase resistance. The current measurement setup limits the endurance test to 10^6 cycles; nevertheless, the device stability at higher pulse energy for 10^6 cycles is still promising. Higher applied energies were found to result in the growth of large ZB GaSb grains through the thickness of the PCM film and failing in the low-resistance state. This failure mode is quite distinctive for the two-phase crystal structure and should be further studied.

The resistance drift [Fig. 8(c)] for $Ga_{0.4}Sb_{0.6}$ was tested for different programmed states prepared from RESET states as in Fig. 8(a) after 10^6 reversible cycles. The resistance drift plots were fitted with the power law equation: $R = R_o{}^*t^\nu$ to obtain the drift coefficient ν. $Ga_{0.2}Sb_{0.8}$ and $Ga_{0.3}Sb_{0.7}$ showed similar resistance drift coefficients (not shown here). As GST PCM cells typically show a power law exponent between $\nu = 0.04$ and 0.1,[40–42] the obtained values from $Ga_{0.4}Sb_{0.6}$, alloy are comparable to GST and show a great promise for programming multiple resistance states. In fact, the drift ν-values from Fig. 8(c) allow for discrete programming of 18 states for a data retention time of 10^7 s at room temperature.

Ga–Sb-based alloys as compared to GST and Te-free PCM demonstrate similar or improved resistance contrast as well as improved drift and endurance up to 10^6 cycles even programming the devices with higher switching energies.[43–46] High-resistance contrast, low-resistance drift coefficients, and high endurance of these alloys provide a potential of engineering Ga–Sb alloy-based cells for multilevel memory devices.

E. Microstructure and chemical changes after reversible switching

Multiple PCM cell cycling likely causes the modification of the microstructure of the PCM alloy, particularly in the current case with phase separation following a very simple equilibrium phase diagram of this binary alloy, containing just three phases: rhombohedral Sb (A7), cubic GaSb (ZB), and orthorhombic metallic Ga, all with negligible mutual solid solubilities.[47]

Figure 9 presents the cross-sectional dark-field (DF) TEM images of 20 nm thick $Ga_{0.2}Sb_{0.8}$ cells after about 100 cycles of reversible switching and left in three states: high-resistance RESET state at 120 kΩ, partial SET or intermediate state at 30 kΩ, and low-resistance SET state at 1.2 kΩ that includes about 500 Ω series access resistance. DF images reveal grains close to Bragg conditions with bright contrast, therefore showing just a few grains in each micrograph. The insets present Fourier power spectra from lattice images of the device regions showing atomic periodicities due to the crystallization of the material.

The RESET state [Fig. 9(a)] shows an almost entirely amorphous cell with ∼20 nm localized crystalline region marked with arrow at the left edge of the TiN plug. This region is further

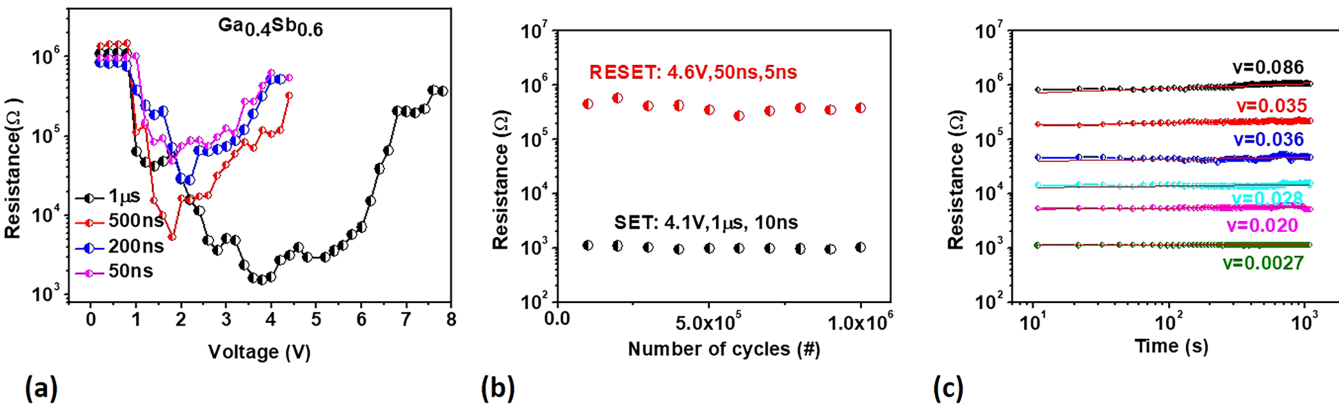

FIG. 8. Characteristics of 16 nm thick $Ga_{0.4}Sb_{0.6}$ mushroom cell: (a) programming R–V curves for different pulse widths with rising and trailing slopes of 10 ns. In each cycle, the cell is initialized in the reset state. (b) RESET and SET state resistance for a total of 10^6 switching cycles. (c) Resistance drift after 10^6 cycles for different resistance states achieved by switching from the RESET state as in (a). Values for the power law exponents, ν, are fitted for each curve.

Published under an exclusive license by AIP Publishing

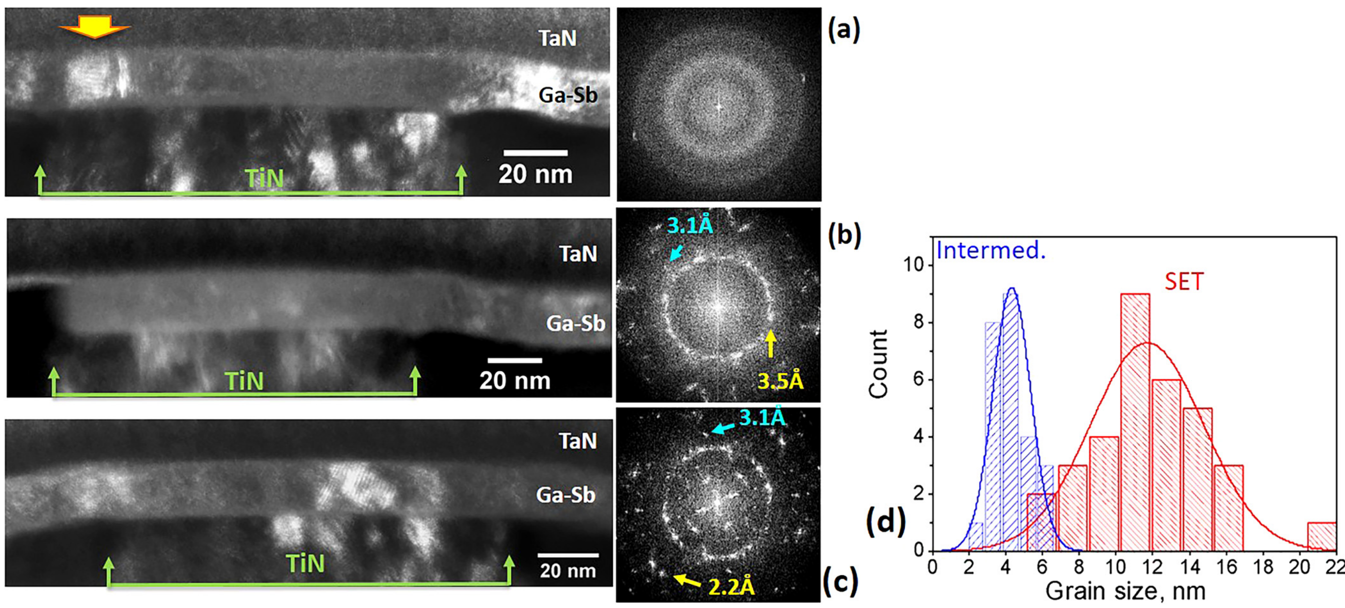

FIG. 9. Cross-sectional dark-field TEM images of ∼20 nm $Ga_{0.2}Sb_{0.8}$ PCM cells and Fourier power spectra from high-resolution lattice images of the PCM above the TiN plug: (a) device in the RESET state (R∼1.2×10^5 Ω), (b) device in the partial SET (intermediate state) (3.0×10^4 Ω), and (c) device in the SET state (1.2×10^3 Ω). Position of the TiN plug is shown with arrows. Reflection of the ZB GaSb phase, d(111) = 3.52 Å, d(220) = 2.15 Å, and A7 Sb phase d(012) = 3.10 Å are marked with arrows. (d) Histogram of grain sizes obtained from multiple DF images.

magnified in Fig. 10. The PCM layer in the Intermediate state appears crystalline with a significantly smaller grain size than in the SET state [Fig. 9(b)]. It is visible in both DF images and finer ring pattern in the Fourier spectra. The most intense rings in both spectra correspond to the (111) reflections of the ZB GaSb phase with 3.52 Å spacing. The strongest reflections of the A7 phase, (012) of 3.10 Å spacing are also visible, revealing phases separated into two crystalline phases.

The grain size distributions were evaluated by image particle analysis from 5–7 DF images collected with different beam tilts. The histograms of grain sizes in the SET and Intermediate states are presented in Fig. 9(d). Upon switching from high-resistance amorphous state, the PCM layer undergoes crystallization, which can be controlled by the amount of applied energy. As a result, the grain size in the intermediate state is averaged at 5 nm, while further programming to the SET state results in the grain growth to about 12 nm [Fig. 9(d)]. It should be noted that the PCM layer thickness was chosen to be small enough compared to the device lateral size to reduce 3D geometrical effects. In this geometry, likely due to the low vertical temperature gradient, grain crystallization appears relatively uniform throughout the film thickness.

Figure 10 magnifies a small ∼20 nm region with crystalized grains in the mostly amorphous film in the RESET state as shown in Fig. 7(a). The grains are separated from the TiN plug with a thin (3–5 nm) amorphous layer resembling the mushroom-type structure. The crystalline region consists mostly of large (5–10 nm) ZB GaSb grains with a few A7 grains as illustrated by the Fourier power spectrum. The Energy Dispersive Spectroscopy (EDS) profile through the film thickness shows approximately Ga:Sb = 44:56 atomic ratio with excess Sb in the amorphous region reduced at least to 37:63. As compared to Te-rich GST material where upon crystallization Sb agglomerates within the heated region leading to

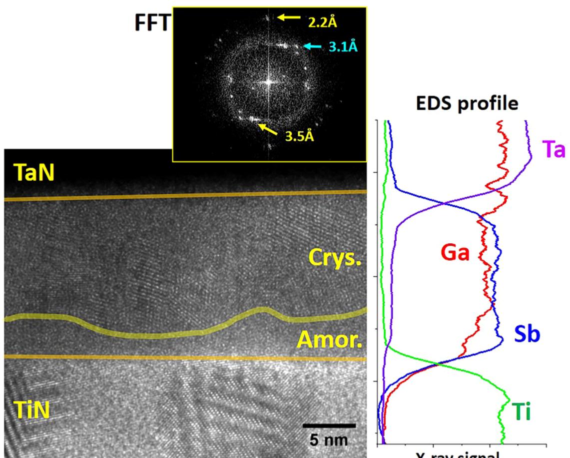

FIG. 10. High-resolution TEM image of a crystallized zinc-blende GaSb in RESET state separated from the TiN plug by 3–5 nm thick amorphous layer along with EDS line intensity profile through the device structure showing reduced Ga content in the amorphous region.

Published under an exclusive license by AIP Publishing

crystallization-induced segregation, the Ga–Sb alloy does not show significant accumulation of Sb or significant chemical changes after multiple reversible cycling.[9]

One of the expected changes, namely, the formation of regions with close to 1:1 binary composition is due to the higher melting temperature of the GaSb phase making ZB grains more stable. Observation of the large GaSb grains in a device in the high-resistance state verifies the ability of device operation with melting/quenching of a small Sb-rich volume of the device keeping ZB grains in a crystalline state.

IV. DISCUSSION: EFFECT OF ALLOY COMPOSITION

Pure amorphous Sb is unstable against crystallization even at room temperature. However, some efforts of using pure Sb as a phase change material by attaining ultrafast cooling from the melt to obtain resistance change have been shown previously.[13] Here, alloying with Ga (as with other group III and IV elements) is known to stabilize Sb amorphous phase at room temperature.[15,36] As evidenced from EXAFS results (Fig. 6), the tetrahedral $Ga–Sb_4$ coordination is mostly responsible for the stabilization of the amorphous network likely due to the rigidity of shorter Ga–Sb chemical bonds. As the equilibrium solubility of Ga in Sb is negligible, annealing causes phase separation into rhombohedral Sb (A7) and zinc-blende GaSb crystal phases. Although the hot plate annealing experiments (Fig. 2) show limited to ∼10 at. % concentration of Ga in the A7 phase, fast and higher temperature annealing in a PCM cell leaves the A7 phase more oversaturated with Ga. This allows for control of RESET resistance, crystallization temperature, and required power of SET pulses. The crystallization mechanism in close-to-equilibrium conditions is revealed by *in situ* XRD studies (Fig. 4). For low Ga concentrations, nucleation of the A7 phase occurs before the ZB cubic phase and is associated with the expulsion of excess Ga from slowly growing grains. This process is relatively slow as it is associated with solid-state diffusion. An order-of-magnitude estimation of this process with time $\tau = 140$ s needed for heating $Ga_{0.1}$-$Sb_{0.9}$ layer from 200 to 300 °C and with diffusion length close to the grain size of $L = 15$ nm, gives a diffusion coefficient of $D \approx L^2/\tau \sim 10^{-14}$ cm^2/s, quite reasonable for solid-state diffusion in substitutional alloys above half-melting temperature.[48]

In pulsed (SET) annealing, pulse energy and duration will determine the composition and grain size of the crystalline A7 phase and, therefore, cell resistance. A simple estimation of the full SET process (Fig. 6) with a pulse width of $\tau = 1\,\mu$s resulting in grain size of $L\sim10$ nm, requires the diffusion coefficient order of magnitude of $D \approx L^2/\tau \sim 10^{-6}$ cm^2/s. Although this value looks extremely high for solid-state diffusion and can be observed only close to the melting point, it was, in fact, estimated for components diffusion in GST just at 320 °C.[49] In a real cell, the diffusion lengths of ∼1 nm should be sufficient for composition control, thus giving a more realistic diffusion coefficient of 10^{-8} cm^2/s. This value can be obtained from Arrhenius extrapolation to 530 °C, with 2.0 eV activation energy from the diffusion coefficient of 10^{-14} cm^2/s estimated above. In any case, the slow Ga out-diffusion component in the partial SET process is an essential asset for the control of resistance of multilevel or analog cells. Contrary to the more traditional volume or thickness control of the amorphous phase,[50] this Ga–Sb system has another programmed property, namely, Ga composition profile in the amorphous phase. Due to the diffusive nature of this programming, the cell resistance strongly depends on pulse annealing time [Fig. 8(a)].

Furthermore, phase separation into the higher melting point GaSb ZB phase and Sb A7 phase provides a route for the reverse process, namely, enrichment of the amorphous phase with Ga. This happens when the RESET pulse is chosen to melt just the A7 grains allowing for dissolved GaSb at the interfaces to diffuse into the melt. The process involves fast diffusion in a liquid phase and is not limited by the duration of RESET pulses down to ∼10 ns. High-power RESET pulses can melt the entire material in a cell and intermix components, thus initializing the cell, but subsequent annealing brings the cell back to the two-phase system which can be further controlled by melting/quenching just the A7 phase.

V. CONCLUSION

The Ga–Sb binary alloy material system shows potential for analog phase change memory applications and was demonstrated to undergo phase change resistive switching in alloys with a Ga concentration of 10–45 at. %. The controllable high crystallization temperature ranging from 180 to 264 °C with high activation energy up to 2.5 eV and retention up to 149 °C for ten years for these alloys indicates higher thermal stability and reliability than the widely used $Ge_2Sb_2Te_5$ compound. XRD studies showed phase separation upon crystallization into two phases, Ga-doped A7 antimony and cubic zinc-blende GaSb. The crystallization into the A7 phase is accompanied by Ga out-diffusion from the grains. EXAFS studies of the local structure of these alloys demonstrated a bond length decrease with a stable coordination number of 4 upon amorphous-to-crystalline phase transformation. Reversible switching for different compositions with RESET/SET resistance ratio of >100 and with RESET switching times as low as 50 ns was demonstrated. TEM and EDS studies of the Ga–Sb cells after ∼100 switching cycles revealed that partial SET or intermediate resistance states are attained by variation of the grain size of the material as well as the Ga content in the A7 phase. Widely controllable crystallization temperature, higher amorphous phase stability, and a possibility of composition control for resistance state programming make Te-free Ga–Sb binary alloys a promising candidate for analog PCM device applications.

ACKNOWLEDGMENTS

This work was supported by the Semiconductor Research Corporation (Task 2960) and the SUNY-IBM AI Collaborative Research Alliance. XAFS analysis by AIF was supported by the National Science Foundation under Grant No. DMR 1911592. This research used beamline 7-BM (QAS) of the National Synchrotron Light Source II, a U.S. DOE Office of Science User Facility operated for the DOE Office of Science by Brookhaven National Laboratory (BNL) under Contract No. DE-SC0012704. The QAS beamline operations were supported in part by the Synchrotron Catalysis Consortium (U.S. DOE, Office of Basic Energy Sciences, Grant No. DE-SC0012335). The authors would like to acknowledge Steven Ehrlich and Lu Ma of 7-BM for their technical assistance.

Published under an exclusive license by AIP Publishing

AUTHOR DECLARATIONS

Conflict of Interest

The authors have no conflicts to disclose.

Author Contributions

Rubab Ume: Conceptualization (equal); Data curation (equal); Formal analysis (equal); Writing – original draft (lead); Writing – review and editing (lead). **Haibo Gong:** Data curation (supporting); Methodology (supporting). **Vadim Tokranov:** Data curation (supporting); Methodology (supporting). **Michael Yakimov:** Investigation (supporting); Project administration (supporting); Resources (supporting). **Kevin Brew:** Conceptualization (supporting); Funding acquisition (equal); Investigation (equal). **Guy Cohen:** Funding acquisition (equal); Investigation (supporting); Supervision (supporting). **Christian Lavoie:** Data curation (supporting); Resources (supporting). **Sandra Schujman:** Data curation (supporting); Methodology (supporting). **Jing Liu:** Data curation (supporting). **Anatoly I. Frenkel:** Data curation (supporting); Resources (supporting). **Karsten Beckmann:** Resources (supporting). **Nathaniel Cady:** Resources (supporting). **Serge Oktyabrsky:** Conceptualization (equal); Formal analysis (supporting); Investigation (lead); Project administration (lead); Resources (supporting); Supervision (lead); Writing – review and editing (equal).

DATA AVAILABILITY

The data that support the findings of this study are available from the corresponding author upon reasonable request.

REFERENCES

[1] B. Lee, P. Zhou, J. Yang, J. Y. Zhang, B. Zhao, E. Ipek, and D. Burger, "Phase-change technology and the future of main memory," IEEE Micro **30**, 143–143 (2010).

[2] D. Ielmini and A. L. Lacaita, "Phase change materials in non-volatile storage," Mater. Today **14**, 600–607 (2011).

[3] G. Burr, M. Breitwisch, M. Franceschini, D. Garetto, K. Gopalakrishnan, B. Jackson *et al.*, "Phase change memory technology," J. Vac. Sci. Technol. B **28**, 223–262 (2010).

[4] A. Lacaita and A. Redaelli, "The race of phase change memories to nanoscale storage and applications," Microelectron. Eng. **109**, 351–356 (2013).

[5] M. Wuttig and N. Yamada, "Phase-change materials for rewriteable data storage," Nat. Mater. **6**, 824–832 (2007).

[6] E. Varesi, A. Modelli, P. Besana, T. Marangon, F. Pellizzer, A. Pirovano, and R. Bez, "Advances in phase change memory technology," in *Proceedings of European Symposium on Phase-Change and Ovonic Sciences* (Balzers, 2004).

[7] F. Ottogalli, A. Pirovano, F. Pellizzer, M. Tosi, P. Zuliani, P. Bonetalli, and R. Bez, "Phase-change memory technology for embedded applications," in *Proceedings of the 30th European Solid-State Circuits Conference* (IEEE, 2004), pp. 293–296.

[8] G. Burr, M. Brightsky, A. Sebastian, H. Cheng, J. Wu, S. Kim, and C. Lam, "Recent progress in phase-change memory technology," IEEE J. Emerg. Sel. Top. Circuits Syst. **6**, 146–162 (2016).

[9] A. Padilla, G. Burr, C. Rettner, T. Topuria, P. Rice, B. Jackson, and B. Kurdi, "Voltage polarity effects in $Ge_2Sb_2Te_5$-based phase change memory devices," J. Appl. Phys. **110**, 054501 (2011).

[10] S. Privitera, E. Rimini, C. Bongiorno, R. Zonca, A. Pirovano, and R. Bez, "Crystallization and phase separation in $Ge_{2+x}Sb_2Te_5$ thin films," J. Appl. Phys. **94**, 4409–4413 (2003).

[11] S. Oh, K. Baek, S. Son, K. Song, J. Oh, S. Jeon, and K. Lee, "*In situ* TEM observation of void formation and migration in phase change memory devices with confined nanoscale $Ge_2Sb_2Te_5$," Nanoscale Adv. **2**, 3841–3848 (2020).

[12] M. Boniardi, A. Redaelli, I. Tortorelli, S. Lavizzari, A. Pirovano, F. Pellizzer, and R. Bez, "Electrical and thermal behavior of tellurium poor GeSbTe compounds for phase change memory," in *2012 4th IEEE International Memory Workshop* (IEEE, 2012), pp. 1–3.

[13] M. Salinga, B. Kersting, I. Ronneberger, V. P. Jonnalagadda, X. T. Vu, M. Le Gallo, I. Giannopoulos, O. Cojocaru-Mirédin, R. Mazzarello, and A. Sebastian, "Monatomic phase change memory," Nat. Mater. **17**, 681–685 (2018).

[14] M. Putero, M. Coulet, T. Ouled-Khachroum, C. Muller, C. Baehtz, and S. Raoux, "Unusual crystallization behavior in Ga-Sb phase change alloys," Appl. Mater. **1**, 062–101 (2013).

[15] L. Van Pieterson, M. Van Schijndel, J. C. N. Rijpers, and M. Kaiser, "Te-free, Sb-based phase-change materials for high-speed rewritable optical recording," Appl. Phys. Lett. **83**, 1373–1375 (2003).

[16] X. Zhou, L. Wu, Z. Song, F. Rao, K. Ren, C. Peng, and S. Feng, "Phase transition characteristics of Al-Sb phase change materials for phase change memory application," Appl. Phys. Lett. **103**, 072–114 (2013).

[17] S. Yoon, N. Lee, S. Ryu, K. Choi, Y. Park, S. Lee, and M. Wuttig, "Sb-Se-based phase-change memory device with lower power and higher speed operations," IEEE Electron Device Lett. **27**, 445–447 (2006).

[18] M. Kang, S. Choi, D. Wamwangi, K. Wang, C. Steimer, and M. Wuttig, "Structural transformation of Sb_xSe_{100-x} thin films for phase change nonvolatile memory applications," J. Appl. Phys. **98**, 014–904 (2005).

[19] T. Zhang, Z. Song, F. Wang, B. Liu, S. Feng, and B. Chen, "Advantages of SiSb phase-change material and its applications in phase-change memory," Appl. Phys. Lett. **91**(22), 222102 (2007).

[20] W. K. Njoroge and M. Wuttig, "Crystallization kinetics of sputter-deposited amorphous AgInSbTe films," J. Appl. Phys. **90**, 3816–3821 (2001).

[21] R. Detemple, D. Wamwangi, M. Wuttig, and G. Bihlmayer, "Identification of Te alloys with suitable phase change characteristics," Appl. Phys. Lett. **83**, 2572–2574 (2003).

[22] L. Van Pieterson, M. H. R. Lankhorst, M. Van Schijndel, A. E. T. Kuiper, and J. H, J. Roosen, "Phase-change recording materials with a growth-dominated crystallization mechanism: A materials overview," J. Appl. Phys. **97**, 083520 (2005).

[23] R. Ume, H. Gong, V. Tokranov, M. Yakimov, D. Sadana, K. Brew, G. Cohen *et al.*, "Crystallization properties of Al-Sb alloys for phase change memory applications," ECS J. Solid State Sci. Technol. **10**(7), 075008 (2021).

[24] K. Ding, J. Wang, Y. Zhou, H. Tian, L. Lu, R. Mazzarello, C. Jia, W. Zhang, F. Rao, and E. Ma, "Phase-change heterostructure enables ultralow noise and drift for memory operation," Science **366**(6462), 210–215 (2019).

[25] Q. Yin and L. Chen, "Crystallization behavior and electrical characteristics of Ga–Sb thin films for phase change memory," Nanotechnology **31**, 215–709 (2020).

[26] A. Gheorghiu, T. Rappeneau, J. P. Dupin, and M. L. Theye, "Electronic properties of flash-evaporated amorphous GaSb films," J. Phys. Colloq. **42**, C4-881–C4-884 (1981).

[27] S. Shun, K. Dropiewski, S. Madisetti, V. Tokranov, M. Yakimov, S. Oktyabrsky, S. Bentley, R. Galatage, and A. Jacob, "Electrical properties related to growth defects in metamorphic GaSb films on Si," J. Vac. Sci. Technol. B **35**, 011203 (2017).

[28] H. E. Kissinger, "Reaction kinetics in differential thermal analysis," Anal. Chem. **29**, 1702–1706 (1957).

[29] L. Kang and L. Chen, "Overview of the role of alloying modifiers on the performance of phase change memory materials," J. Electron. Mater. **50**(1), 1–24 (2021).

[30] C. S. Barrett, P. Cucka, and K. Haefner, "The crystal structure of antimony at 4.2, 78 and 298 K," Acta Crystallogr. **16**, 451–453 (1963).

[31] A. Velea, C. N. Borca, G. Socol, A. C. Galca, D. Grolimund, M. Popescu, and J. A. van Bokhoven, "*In-situ* crystallization of GeTe/GaSb phase change memory stacked films," J. Appl. Phys. **116**, 234306 (2014).

Published under an exclusive license by AIP Publishing

[32]P. S. Dutta, H. L. Bhat, and V. Kumar, "The physics and technology of gallium antimonide: An emerging optoelectronic material," J. Appl. Phys. **81**, 5821–5870 (1997).
[33]T. G. Edwards, I. Hung, Z. Gan, B. Kalkan, S. Raoux, and S. Sen, "Structural transformations in amorphous ↔ crystalline phase change of Ga-Sb alloys," J. Appl. Phys. **114**, 233512 (2013).
[34]B. Ravel and M. Newville, "ATHENA, ARTEMIS, HEPHAESTUS: Data analysis for x-ray absorption spectroscopy using IFEFFIT," J. Synchrotron Radiat. **12**, 537–541 (2005).
[35]A. Kossoy, Q. Wang, R. Korobko, V. Grover, Y. Feldman, E. Wachtel, A. K. Tyagi, A. I. Frenkel, and I. Lubomirsky, "Evolution of the local structure at the phase transition in CeO_2-Gd_2O_3 solid solutions," Phys. Rev. B **87**, 054101 (2013).
[36]A. V. Sapelkin, S. C. Bayliss, A. G. Lyapin, V. V. Brazhkin, and A. J. Dent, "Structure of bulk amorphous GaSb: A temperature-dependent EXAFS study," Phys. Rev. B **56**, 11531 (1997).
[37]I. Ronneberger, Y. Chen, W. Zhang, and R. Mazzarello, "Local structural origin of the crystallization tendency of pure and alloyed Sb," Phys. Status Solidi (RRL) **13**, 1800552 (2019).
[38]B. Kalkan, T. G. Edwards, S. Raoux, and S. Sen, "Nature of metastable amorphous-to-crystalline reversible phase transformations in GaSb," J. Chem. Phys. **139**, 084507 (2013).
[39]C.-C. Chang, C.-T. Chao, J.-C. Wu, T.-R. Yew, M.-J. Tsai, and T.-S. Chin, "The use of $Ga_{16}Sb_{84}$ alloy for electronic phase-change memory," Scr. Mater. **64**, 801–804 (2011).
[40]M. Boniardi, A. Redaelli, A. Pirovano, I. Tortorelli, D. Ielmini, and F. Pellizzer, "A physics-based model of electrical conduction decrease with time in amorphous $Ge_2Sb_2Te_5$," J. Appl. Phys. **105**, 084506 (2009).
[41]J. L. M. Oosthoek, D. Krebs, M. Salinga, D. J. Gravesteijn, G. A. M. Hurkx, and B. J. Kooi, "The influence of resistance drift on measurements of the activation energy of conduction for phase-change material in random access memory line cells," J. Appl. Phys. **112**, 084506 (2012).
[42]I. V. Karpov, M. Mitra, D. Kau, G. Spadini, Y. A. Kryukov, and V. G. Karpov, "Fundamental drift of parameters in chalcogenide phase change memory," J. Appl. Phys. **102**, 124503 (2007).
[43]Y. Lu, S. Song, Z. Song, D. Yao, W. Xi, W. Yin, H. Zheng, and S. Feng, "Phase change memory based on $(Sb_2Te_3)_{0.85}$–$(HfO_2)_{0.15}$ composite film," Appl. Phys. Express **3**(11), 111201 (2010).
[44]Y. Lu, S. Song, Y. Gong, Z. Song, F. Rao, L. Wu, B. Liu, and D. Yao, "Ga-Sb-Se material for low-power phase change memory," Appl. Phys. Lett. **99**(24), 24311 (2011).
[45]K. Ding, F. Rao, M. Xia, Z. Song, L. Wu, and S. Feng, "The impact of W doping on the phase change behavior of Sb_2Te_3," J. Alloys Compd. **688**, 22–26 (2016).
[46]Y. Zhu, Z. Zhang, S. Song, H. Xie, Z. Song, X. Li, L. Shen, L. Li, L. Wu, and B. Liu, "Ni-doped GST materials for high speed phase change memory applications," Mater. Res. Bull. **64**, 333–336 (2015).
[47]T. L. Ngai, R. C. Sharma, and Y. A. Chang, "The Ga–Sb (gallium–antimony) system," Bull. Alloy Phase Diagr. **9**, 586–591 (1988).
[48]A. Van der Ven, H. C. Yu, G. Ceder, and K. Thornton, "Vacancy mediated substitutional diffusion in binary crystalline solids," Prog. Mater. Sci. **55**, 61–105 (2010).
[49]D. Loke, T. H. Lee, W. J. Wang, L. P. Shi, R. Zhao, Y. C. Yeo *et al.*, "Breaking the speed limits of phase-change memory," Science **336**, 1566–1569 (2012).
[50]N. Papandreou, A. Pantazi, A. Sebastian, E. Eleftheriou, M. Breitwisch, C. Lam *et al.*, "Estimation of amorphous fraction in multilevel phase-change memory cells," Solid-State Electron. **54**, 991–996 (2010).

Published under an exclusive license by AIP Publishing